Journal of Power Sources 196 (2011) 10019–10031

Contents lists available at ScienceDirect

Journal of Power Sources

journal homepage: www.elsevier.com/locate/jpowsour

Computational modeling of microfluidic fuel cells with flow-through porous electrodes

Deepak Krishnamurthy[a,b], Erik O. Johansson[a,c], Jin Wook Lee[a], Erik Kjeang[a,*]

[a] Mechatronic Systems Engineering, School of Engineering Science, Simon Fraser University, 250-13450 102 Avenue, Surrey, BC V3T 0A3, Canada
[b] Department of Mechanical Engineering, Birla Institute of Technology and Science, Pilani, Rajasthan 333031, India
[c] Department of Applied Physics and Electronics, Umeå University, Umeå, SE-90187, Sweden

ARTICLE INFO

Article history:
Received 19 July 2011
Received in revised form 3 August 2011
Accepted 4 August 2011
Available online 11 August 2011

Keywords:
Microfluidic
Fuel cell
Flow-through
Porous electrode
Modeling

ABSTRACT

In the current work, a computational model of a microfluidic fuel cell with flow-through porous electrodes is developed and validated with experimental data based on vanadium redox electrolyte as fuel and oxidant. The model is the first of its kind for this innovative fuel cell design. The coupled problem of fluid flow, mass transport and electrochemical kinetics is solved from first principles using a commercial multiphysics code. The performance characteristics of the fuel cell based on polarization curves, single pass efficiency, fuel utilization and power density are predicted and theoretical maxima are established. Fuel and oxidant flow rate and its effect on cell performance is considered and an optimal operating point with respect to both efficiency and power output is identified for a given flow rate. The results help elucidate the interplay of kinetics and mass transport effects in influencing porous electrode polarization characteristics. The performance and electrode polarization at the mass transfer limit are also detailed. The results form a basis for determining parameter variations and design modifications to improve performance and fuel utilization. The validated model is expected to become a useful design tool for development and optimization of fuel cells and electrochemical sensors incorporating microfluidic flow-through porous electrodes.

1. Introduction

Microscale power sources are currently under rapid development due to the high demand for use in small, portable applications. These applications include personal electronic devices such as mobile phones, laptops as well as wireless sensors, global positioning systems, medical diagnostics and other specialized devices. Next generation power sources serving these applications are required to be light weight, have high power densities, high durability and long periods of operation between recharge. Miniature fuel cells [1–3] have shown great promise as power sources for small-scale applications due to their inherently high power and energy density. However, scaling down conventional fuel cell technologies to produce miniature power sources has several challenges. Mechanical constraints arise due to limitations in graphite plate size that can be machined, and miniaturization decreases the structural strength of the membrane electrode assembly. Furthermore, hydrogen based fuel cells require hydrogen storage units that are generally too bulky for portable applications. Direct liquid fuel cells on the other hand suffer low cell voltage due to slow electrochemical kinetics and fuel crossover. There are also noteworthy challenges associated with membrane hydration and degradation common to all polymer electrolyte membrane fuel cell technologies.

A recent, novel fuel cell architecture based on microfluidic lab-on-chip devices has shown great promise in addressing many of the above problems. These microfluidic or laminar flow based fuel cells incorporate all the fundamental components of a conventional fuel cell to a microfluidic channel and its walls [4]. Such fuel cells operate without a membrane and in the most common configuration use the laminar nature of microscale flows to maintain separation between fuel and oxidant streams, and at the same time facilitate ionic charge transfer. Crossover effects are eliminated by strategic cell design provided that interdiffusion is restricted to a small interfacial width at the center channel, from which the electrodes are positioned sufficiently far away. In this way, microfluidic fuel cells prove to have a number of unique advantages [4,5]: the need for an ion-exchange membrane is eliminated and along with it the membrane related issues; sealing, manifolding and fuel delivery system requirements are reduced; manufacturing of these fuel cells using

* Corresponding author. Tel.: +1 778 782 8791; fax: +1 778 782 7514.
E-mail address: ekjeang@sfu.ca (E. Kjeang).

0378-7753/$ – see front matter © 2011 Elsevier B.V. All rights reserved.
doi:10.1016/j.jpowsour.2011.08.024

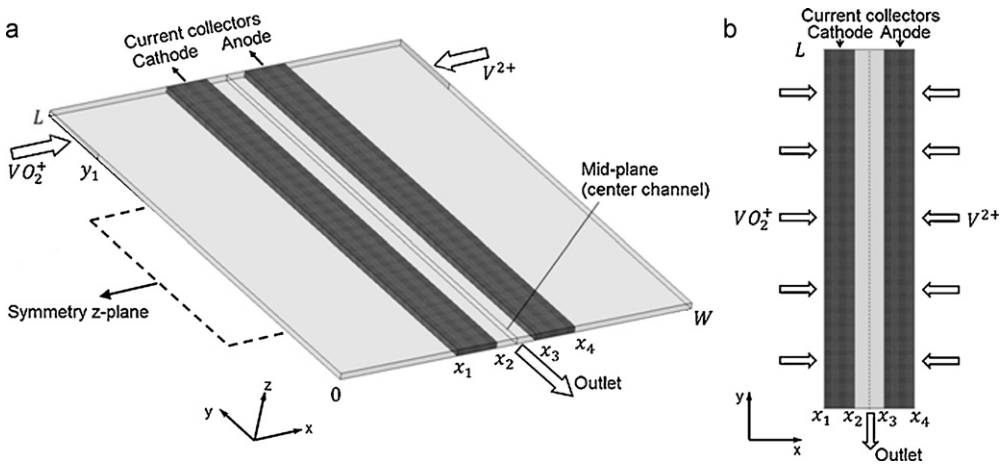

Fig. 1. Schematic of the microfluidic fuel cell with flow-through porous electrodes, showing the 3D and 2D modeling domains in parts (a) and (b), respectively.

established microfabrication methods is inexpensive [6]; and they can operate at room temperature and do not require any auxiliary systems for water management and cooling.

Notwithstanding these advantages, as with any emerging technology, many challenges and opportunities for improvement exist. The lack of fuel distribution is an important consideration for microfluidic fuel cells as well as other miniaturized fuel cells, and other issues such as sealing arise due to use of liquid fuels and electrolytes. However, microfluidic fuel cells with flow-through porous electrodes can conveniently be recharged *in situ* by running the cell in electrolytic mode [7] in a closed-loop system, thus eliminating the need for frequent refueling. Moreover, although recharging is expected to be slower than manually replacing a fuel cartridge, it can potentially be faster than for conventional batteries due to the convective mass transport of the flow-through cell architecture. On the system level, microfluidic fuel cells require a pump to operate. While vanadium redox based electrochemical cells have relatively high durability [8], the pump may have a negative effect on overall fuel cell system lifetime and may need to be replaced more frequently than the electrolyte. The cost and parasitic power requirements of the pump are also important to consider for system integration of microfluidic fuel cells. Other challenges include high contact resistances which result from establishing electrical contact between porous electrodes and the external circuit.

A variety of microfluidic fuel cells have been demonstrated using different fuel and oxidant combinations, electrode materials and channel configurations [4]. One of the first such devices was reported by Ferrigno et al. [9], utilizing vanadium species for both half-cells in a Y-shaped microchannel. Using a similar Y-shaped channel design, Choban et al. [10] demonstrated a microfluidic fuel cell running on formic acid as fuel. Cohen et al. [11] introduced the planar or F-shaped microchannel design fuel cell using formic acid as fuel. This design had increased contact area between the electrolyte and electrodes as compared to previous designs. Devices using oxygen as the oxidant suffered from low power densities due to the poor solubility of oxygen in liquid electrolytes. This problem was addressed by Jayashree et al. [12], who introduced the novel, air breathing electrode architecture. All the above mentioned devices were reported to be limited by mass transport to the active sites, and as a result had low fuel utilization and power density values. Kjeang et al. [7,13,14] recently reported incremental design improvements to mitigate this limitation, including graphite rod arrays and porous carbon paper as electrodes, culminating in a microfluidic fuel cell with flow-through porous carbon electrodes using vanadium species in both half-cells. This device has demonstrated some of the highest power density levels (131 mW cm^{-2}) and fuel utilization values (100%) of all the devices reported till date [3–5] along with *in situ* fuel regeneration capabilities. More recently, a few other architectures have been reported by Salloum et al. [15–17] using flow-through electrodes and vanadium species.

Modeling of microfluidic fuel cells is important to cut down the time involved in prototyping, building and characterizing actual devices, and to understand the effect of various design parameters on the performance. Modeling can also elucidate the complex mass transfer and electrochemical coupling effects which exist in these devices. The first Computational Fluid Dynamics (CFD) based model for microfluidic fuel cells was developed by Bazylak et al. [18] who considered a T-shaped microchannel and suggested methods to improve fuel utilization by using tapered electrodes. Chang et al. [19] presented a theoretical model which included a Butler–Volmer model for the electrochemical kinetics in a Y-shaped microchannel. A similar model for the planar or F-shaped channel was reported by Chen et al. [20] and validated based on the experiments performed by Cohen et al. [11]. No theoretical/numerical models have yet been developed for the flow-through electrode architecture.

The overall objective of the present work is to develop and validate a detailed computational model for a microfluidic fuel cell with flow-through porous electrodes. The model incorporates all the fundamental phenomena in the fuel cell including fluid flow in microchannels and porous media, mass transport and electrochemical kinetics, and resolves the characteristics of both individual half-cells (anode and cathode) as well as the combined fuel cell. Such a model is expected to be a vital tool to understand the unique physicochemical characteristics of this configuration and to support the development and optimization of cell architectures. Results are expected to shed light on electrode polarization characteristics and guide the design of higher performance electrode architectures. In addition, this work is intended to provide a general numerical modeling framework for electrochemical devices with microfluidic flow-through architectures, such as microfluidic bio-sensors.

2. Model formulation and theory

The microfluidic fuel cell architecture considered in this work is based on vanadium redox reactions at both half-cells and incorporates porous flow-through carbon paper electrodes [7]. A full numerical description of all fundamental transport and reaction phenomena occurring in the fuel cell is highly complex with a large degree of non-linearity, and to obtain a solution it is necessary to simplify the problem to a manageable level. In order to present a

straightforward yet accurate model, the main assumptions made are listed below:

1. Isothermal and steady state conditions are considered.
2. Incompressible fluid flow is assumed and effects of gravity are neglected.
3. Physical properties of the electrode and electrolyte are considered homogeneous.
4. Dilute solution approximation is assumed to hold.
5. Ionic migration is neglected owing to the high concentrations of supporting electrolyte.

Assumptions 4 and 5 are justified owing to the aqueous, acidic nature of the electrolyte used in [7] and modeled here. Apart from these general assumptions, others regarding the electrochemical kinetics and mass transport aspects of the model will be detailed in following sections as they arise.

2.1. Geometry

A schematic of the fuel cell indicating the modeling domain is shown in Fig. 1. The electrolyte streams enter the fuel cell via the two inlets on either side, and after passing through the inlet reservoirs, flow through the porous electrodes. The two streams exit the electrodes into the common center channel where they make a 90° turn and flow in a stratified, co-laminar format towards the outlet. The channel thickness is constant at 300 μm. Due to plug flow conditions in the porous electrodes, it is deemed sufficient to model a two dimensional (2D) slice for the mass transport and electrochemistry. However, variations in flow velocity at the entrance to the electrodes along their length (y direction) are expected. For effectively capturing the flow distribution, the fluid flow is solved using a full three dimensional (3D) model of the cell. The resulting 3D calculations are used to define the fluid flow boundary conditions at the inlet of the electrodes in the 2D model. The domain used for 3D modeling is shown in Fig. 1(a) and the same for the 2D model in Fig. 1(b). Note that the cell is bisected along the channel thickness for the 3D model, to exploit the symmetry about this plane. The position of the current collectors at the end of each electrode is shown in Fig. 1. The mid-plane bisecting the cell width wise is used for half-cell modeling purposes.

2.2. Fluid flow model

A complete 3D, laminar CFD model is used to capture the flow distribution in the fuel cell. The carbon paper electrodes are treated as porous bodies with homogeneous permeability in the in-plane direction. The pressure drop across the electrodes is calculated using the well-known Darcy's law [21]. The continuity and momentum equations, written for regions inside the electrodes are:

$$\nabla \cdot \vec{v} = 0 \tag{1}$$

$$\nabla p = -\frac{\mu}{K}\vec{v} \tag{2}$$

where $\vec{v}$ is the superficial fluid velocity vector, p is the pressure in the liquid, μ is the dynamic viscosity and K is the permeability of the carbon paper in the in-plane direction [22,23]. The incompressible equations for continuity and momentum conservation [21] used for the flow in the regions outside the porous electrodes are given by:

$$\nabla.\vec{v} = 0 \tag{3}$$

$$\frac{\partial \vec{v}}{\partial t} + (\vec{v}.\nabla\vec{v}) = -\frac{1}{\rho}\nabla p + \frac{\mu}{\rho}\nabla^2\vec{v} \tag{4}$$

2.3. Electrochemistry and mass transport model

The governing equations for species conservation and charge conservation in the carbon paper electrode and electrolyte region are written as [24,25]:

$$\vec{v}\nabla c_j - D_j^{eff}\nabla^2 c_j = S_j \tag{5}$$

$$\nabla.\vec{\imath}_s = -\nabla.\vec{\imath}_l = -\sigma_s^{eff}\nabla^2\phi_s = k_l^{eff}\nabla^2\phi_l \tag{6}$$

The variables in Eqs. (5) and (6) are explained as follows: c_j denotes the bulk concentration of the vanadium species j, where $j \in \{II, III, IV$ and $V\}$. The symbols $\{II, III, IV$ and $V\}$ refer to the vanadium species $\{V^{2+}, V^{3+}, VO^{2+}$ and $VO_2^+\}$ respectively, in all the following sections. D_j^{eff} are the effective diffusion coefficients of species j; S_j are the species source terms for the species j; ϕ_s, ϕ_l are the potentials in the electrode and electrolyte, respectively; $\vec{\imath}_s$, $\vec{\imath}_l$ are the electrode and electrolyte current densities; and σ_s^{eff} and k_l^{eff} are the effective conductivities of the electrode and electrolyte, respectively.

Mixed evidence [26–28] exists regarding redox kinetics of vanadium reactions occurring on carbon electrodes. These have been characterized to have a complex mechanism, with combined chemical and electron transfer reactions [26–28], of which the single electron transfer is the rate determining step [26]. Moreover, the exact nature of the solvated vanadium ions has been reported to be dependent on pH and vanadium ion concentration [29]. However, a simplified treatment of the redox kinetics involving single electron transfer reactions has been demonstrated [25] to be sufficient in capturing the qualitative cell behaviour. The overall redox reactions considered here are:

$$VO_2^+ + 2H^+ + e^- \rightleftharpoons VO^{2+} + H_2O, \qquad U_1^0 = 0.750\,V \quad vs \quad SCE \tag{7}$$

$$V^{3+} + e^- \rightleftharpoons V^{2+}, \qquad U_2^0 = -0.496\,V \quad vs \quad SCE \tag{8}$$

where U_1^0 and U_2^0 are the standard equilibrium potentials versus the Saturated Calomel Electrode (SCE) [30]. Other than the primary reactions given above, a secondary reaction involving the V^{3+} and VO^{2+} species is known to occur [31]:

$$VO^{2+} + 2H^+ + e^- \rightleftharpoons V^{3+} + H_2O, \qquad U^0 = 0.07\,V \quad vs \quad SCE \tag{9}$$

During normal operating cell conditions, this reaction has a negligible rate [32] due to slow kinetics and low reactant concentration. Hydrogen and oxygen evolution may also occur as side reactions in the acidic, aqueous electrolyte present in the cell. However, previous studies show that the kinetics of these side reactions is around five orders of magnitude lower than the main vanadium redox reactions (Eqs. (7) and (8)) on carbon electrodes [26,33,34]. Furthermore, during typical fuel cell operation the local overpotentials are not high enough for these reactions to occur. Therefore from thermodynamic and kinetics considerations at leading order the effect of these reactions is negligible and consequently not included in the model.

Experimental investigations by Fabjan et al. [26] into the vanadium redox kinetics have shown that a single electron transfer is the rate determining step, making it amenable to a Butler–Volmer [35,36] model. Other works [27,28] suggest an alternative mechanism for the VO^{2+}/VO_2^+ couple. Several earlier modeling efforts of vanadium redox batteries [25,37] have shown that performance of a cell based on these reactions is adequately captured by the Butler–Volmer equation. Therefore, given the uncertainties that exist with regards to the kinetics of the vanadium redox reactions, the Butler–Volmer equation [35,36] is deemed a necessary and justified simplification for the present model. The charge transfer

current densities corresponding to the redox reactions are thus given by:

$$i_1 = i_1^0 \left\{ \frac{c_{IV}^s}{c_{IV}} \exp\left(\frac{\alpha_{1,a} F\eta_1}{RT}\right) - \frac{c_V^s}{c_V} \exp\left(\frac{-\alpha_{1,c} F\eta_1}{RT}\right) \right\} \quad (10)$$

$$i_2 = i_2^0 \left\{ \frac{c_{II}^s}{c_{II}} \exp\left(\frac{\alpha_{2,a} F\eta_2}{RT}\right) - \frac{c_{III}^s}{c_{III}} \exp\left(\frac{-\alpha_{2,c} F\eta_2}{RT}\right) \right\} \quad (11)$$

Note that subscript 1 refers to the VO^{2+}/VO_2^+ side, which is the cathode during fuel cell operation, and subscript 2 refers to the V^{2+}/V^{3+} side, or the anode. The superscript s refers to the surface concentration of the vanadium species. α is the charge transfer coefficient, with subscripts a and c referring to oxidation (anodic) and reduction (cathodic) reactions, respectively. F is Faraday's constant, R is the universal gas constant, T is the operating temperature and η is the overpotential. The exchange current density i^0 represents the rate of charge transfer when the reaction is at equilibrium. For the cathode and anode side it is written as:

$$i_1^0 = Fk_1 (c_{IV})^{\alpha_{1,c}} (c_V)^{\alpha_{1,a}} \quad (12)$$

$$i_2^0 = Fk_2 (c_{II})^{\alpha_{2,c}} (c_{III})^{\alpha_{2,a}} \quad (13)$$

where k_1 and k_2 are the standard reaction rate constants. The overpotentials at the cathode and anode side are written as:

$$\eta_1 = \phi_s - \phi_l - U_1 \quad (14)$$

$$\eta_2 = \phi_s - \phi_l - U_2 \quad (15)$$

The Nernst equation is used to estimate the half-cell potentials:

$$U_1 = U_1^0 + \frac{RT}{F} \ln\left(\frac{c_V}{c_{IV}}\right) \quad (16)$$

$$U_2 = U_2^0 + \frac{RT}{F} \ln\left(\frac{c_{III}}{c_{II}}\right) \quad (17)$$

i_1 and i_2 are used to define the source terms for the charge conservation equations (Eq. (6)) in the electrode and electrolyte which are given by:

$$\nabla.\vec{i}_s = -\nabla.\vec{i}_l = S_1 = -ai_1 \quad (18)$$

$$\nabla.\vec{i}_s = -\nabla.\vec{i}_l = S_2 = -ai_2 \quad (19)$$

where a is the internal active surface area of the electrode, the value of which is estimated based on fibre diameter and porosity and is listed in Table 3. The vanadium species are transported to and from the electrode surface through the combined effect of convection and diffusion inside the pores of the electrodes. This rate of transport is proportional to the difference in concentration between bulk and the surface and defines the species source terms in Eq. (5) as:

$$S_j = ak_{mj}(c_j^s - c_j), \quad j \in \{II, III, IV \text{ and } V\} \quad (20)$$

where k_{mj} are the mass transfer coefficients for each vanadium species, which depend on the flow velocity and diffusion coefficients of the species. These are estimated using an empirical relationship for mass transfer in carbon fibre electrodes [38]:

$$Sh = 7Re^{0.4}, \quad (56 < Pe < 280) \quad (21)$$

The Sherwood number and Reynolds number are calculated with respect to the carbon fibre diameter (d) and the apparent (superficial) velocity in the porous medium. The Peclet number range used for this study is of the same order of magnitude as the above range, making this a suitable correlation. In the fluidic domain inside the electrodes, these three dimensionless quantities are written as:

$$Re = \frac{\rho|\vec{v}|d}{\mu} \quad (22)$$

$$Sh_j = \frac{k_{mj}d}{D_j} \quad (23)$$

$$Pe_j = \frac{|\vec{v}|d}{D_j} \quad (24)$$

Expanding Eq. (21) for each vanadium species using Eqs. (22)–(24) we can write,

$$k_{mj} = 7\frac{D_j}{d}\left(\frac{\rho|\vec{v}|d}{\mu}\right)^{0.4} \quad (25)$$

This correlation is valid for mass transfer for a single fibre and provides an upper limit for a bundle of fibres. The agreement with experimental data is reported to be within 30% error [38].

Since the redox reactions being modeled are surface based, there is a direct coupling between the mass transport and the electrochemistry. At steady state, the rate at which a chemical species is transported to or from the surface of the carbon fibres equals the rate of the reaction. Hence, the relationship can be expressed mathematically between the mass transport and electrochemical source terms. From Eqs. (18)–(20):

$$S_{IV} = -S_V = \frac{S_1}{F} \quad (26)$$

$$S_{II} = -S_{III} = \frac{S_2}{F} \quad (27)$$

Eqs. (26) and (27) also express the relationship between surface and bulk concentration for the reacting species, and the corresponding overpotential on the anode and cathode side. Rearranging this equation, we can write the surface concentration for each species as a function of the bulk concentrations and overpotentials [25]:

$$c_{IV}^s = \frac{(k_1/k_{mj})(c_{IV})^{\alpha_{1,c}}(c_V)^{1-\alpha_{1,a}} \exp((-\alpha_{1,c}F\eta_1)/RT) + \{1 + (k_1/k_{mj})(c_{IV})^{\alpha_{1,c}}(c_V)^{-\alpha_{1,a}} \exp((-\alpha_{1,c}F\eta_1)/RT)\}c_{IV}}{1 + (k_1/k_{mj})(c_{IV})^{-\alpha_{1,c}}(c_V)^{\alpha_{1,a}} \exp((\alpha_{1,a}F\eta_1)/RT) + (k_1/k_{mj})(c_{IV})^{\alpha_{1,c}}(c_V)^{-\alpha_{1,a}} \exp((-\alpha_{1,c}F\eta_1)/RT)}, \quad j \in IV \quad (28)$$

$$c_V^s = \frac{(k_1/k_{mj})(c_{IV})^{1-\alpha_{1,c}}(c_V)^{\alpha_{1,a}} \exp((-\alpha_{1,a}F\eta_1)/RT) + \{1 + (k_1/k_{mj})(c_{IV})^{-\alpha_{1,c}}(c_V)^{\alpha_{1,a}} \exp((\alpha_{1,a}F\eta_1)/RT)\}c_V}{1 + (k_1/k_{mj})(c_{IV})^{-\alpha_{1,c}}(c_V)^{\alpha_{1,a}} \exp((\alpha_{1,a}F\eta_1)/RT) + (k_1/k_{mj})(c_{IV})^{\alpha_{1,c}}(c_V)^{-\alpha_{1,a}} \exp((-\alpha_{1,c}F\eta_1)/RT)}, \quad j \in V \quad (29)$$

$$c_{II}^s = \frac{(k_2/k_{mj})(c_{II})^{\alpha_{2,c}}(c_{III})^{1-\alpha_{2,a}} \exp((-\alpha_{2,c}F\eta_2)/RT) + \{1 + (k_2/k_{mj})(c_{II})^{\alpha_{2,c}}(c_{III})^{-\alpha_{2,a}} \exp((-\alpha_{2,c}F\eta_2)/RT)\}c_{II}}{1 + (k_2/k_{mj})(c_{II})^{-\alpha_{2,c}}(c_{III})^{\alpha_{2,a}} \exp((\alpha_{2,a}F\eta_2)/RT) + (k_2/k_{mj})(c_{II})^{\alpha_{2,c}}(c_{III})^{-\alpha_{2,a}} \exp((-\alpha_{2,c}F\eta_2)/RT)}, \quad j \in II \quad (30)$$

$$c_{III}^s = \frac{(k_2/k_{mj})(c_{II})^{1-\alpha_{2,c}}(c_{III})^{\alpha_{2,a}} \exp((\alpha_{2,a}F\eta_2)/RT) + \{1 + (k_2/k_{mj})(c_{II})^{-\alpha_{2,c}}(c_{III})^{\alpha_{2,a}} \exp((\alpha_{2,a}F\eta_2)/RT)\}c_{III}}{1 + (k_2/k_{mj})(c_{II})^{-\alpha_{2,c}}(c_{III})^{\alpha_{2,a}} \exp((\alpha_{2,a}F\eta_2)/RT) + (k_2/k_{mj})(c_{II})^{\alpha_{2,c}}(c_{III})^{-\alpha_{2,a}} \exp((-\alpha_{2,c}F\eta_2)/RT)}, \quad j \in III \quad (31)$$

Several works [23,39–43] have determined the mass transport related effective properties of porous media. For TORAY carbon paper, studies by Zamel et al. [39] show that the effective in-plane diffusivity predicted by Bruggeman's correction [43] is within 15% of different experimental and numerical studies [23,39–41]. Inside the carbon paper the effective diffusion coefficients are calculated based on this correction [43]:

$$D_j^{eff} = D_j \varepsilon^{1.5} \quad (32)$$

where ε is the porosity of the carbon paper. The electrolyte conductivity in the microchannels and electrode pores are calculated as:

$$k_l = \frac{F^2}{RT}\sum_j z_j^2 D_j c_j \tag{33}$$

$$k_l^{eff} = \frac{F^2}{RT}\sum_j z_j^2 D_j^{eff} c_j \tag{34}$$

Here, $j \in \{II, III, IV, V \text{ and } H^+\}$ to account for the electrolyte conductivity of the acid. k_l is the electrolyte conductivity outside the electrode regions and z_j is the charge number for each of the ionic species. The proton concentration in the solution is assumed to be constant at 8 M since changes in proton concentration are small during fuel cell operation.

2.4. Boundary conditions and parameters

2.4.1. Fluid flow boundary conditions

In the 3D fluid flow model, the following boundary conditions are used. Since the geometry exhibits symmetry about the half z-plane, we can reduce the model domain by half by implementing a symmetry boundary condition at this plane (Fig. 1(a)):

$$\frac{\partial p}{\partial z} = 0, \qquad \frac{\partial \vec{v}}{\partial z} = 0 \quad at \quad z = 0 \quad for \quad all \quad x \quad and \quad y \tag{35}$$

At the inlet, the inward normal velocity is written as a function of volume flow rate and inlet channel area:

$$\vec{v}\cdot\hat{n} = \begin{cases} \dfrac{V_{in}^0}{a_{in}}, & x = 0, \quad y_1 \le y \le L, \quad 0 \le z \le \dfrac{h}{2} \\ \dfrac{V_{in}^0}{a_{in}}, & x = W, \quad y_1 \le y \le L, \quad 0 \le z \le \dfrac{h}{2} \end{cases} \tag{36}$$

where V_{in}^0 is the inlet volume flow rate for the cathode and anode side, a_{in} is the area of the inlet channel and h is the channel thickness. The outlet is specified as a constant pressure boundary:

$$p = 0\left\{x_2 \le x \le x_3, \qquad y = 0, \qquad 0 \le z \le \frac{h}{2}\right\} \tag{37}$$

For the 2D model, the flow field results from the 3D model are averaged across the channel thickness and mapped as a boundary condition at the inlet to the electrodes. Expressing the above mathematically:

$$\vec{v}\cdot\hat{n} = \begin{cases} F_1(y).\hat{n}, & x = x_1, \quad 0 \le y \le L \\ F_2(y).\hat{n}, & x = x_4, \quad 0 \le y \le L \end{cases} \tag{38}$$

where $F_1(y)$ and $F_2(y)$ represent the flow field solution from the 3D model. Similar to the 3D case, the outlet is specified as a constant pressure boundary:

$$p = 0\{x_2 \le x \le x_3, \qquad y = 0\} \tag{39}$$

2.4.2. Mass transport boundary conditions

Since no electrochemical reactions occur outside the electrodes, the concentration is assumed constant at the inlet for both cathode and anode sides:

$$c_j = c_j^0 \begin{cases} j \in \{IV, V\}, & x = x_1, \quad 0 \le y \le L \\ j \in \{II, III\}, & x = x_4, \quad 0 \le y \le L \end{cases} \tag{40}$$

The high purity vanadium solutions in 4 M H_2SO_4 used in [7] are considered for which $c_V^0 \approx 2$ M, $c_{II}^0 \approx 2$ M. The outlet is specified as a pure convection boundary considering the relatively large velocities compared to other regions in the cell:

$$\frac{\partial c_j}{\partial y} = 0\{x_2 \le x \le x_3, \quad y = 0\} \tag{41}$$

All other boundaries are considered as no-flux or insulation boundaries.

2.4.3. Current conservation boundary conditions

The electric current enters and leaves the fuel cell via the two current collectors at the top end of the carbon paper electrodes. For complete cell modeling purposes, the anode current collector is set to zero potential and the cathode current collector is maintained at a potential which is varied in order to simulate the polarization curves and cell performance:

$$\phi_s = \begin{cases} V_{cell}, & x_1 \le x \le x_2, \quad y = L \\ 0, & x_3 \le x \le x_4, \quad y = L \end{cases} \tag{42}$$

where V_{cell} is the cell voltage. Equivalently, the cathode side may be set to a current density boundary, where the total normal current density from the boundary is varied to simulate cell performance. For half-cell modeling, the electrolyte potential at the center channel is set to zero and the potential at the cathodic/anodic current collector is swept:

$$\phi_s = V_{cell}\{x_1 \le x \le x_2, \qquad y = L \quad or \quad x_3 \le x \le x_4, \qquad y = L\} \tag{43}$$

$$\phi_l = 0\left\{x = \frac{x_2 + x_3}{2}, \quad 0 \le y \le L\right\} \tag{44}$$

All other boundaries are set to insulation boundaries.

2.4.4. Modeling parameters

Mass transfer and electrochemical kinetics parameters are an important part of the numerical model in the current work. Identification of relevant and accurate values for these is closely related to model accuracy. A thorough search of the literature reporting experimental measurements was conducted to ascertain the parameter values. The experimental works in literature [29,44–50] were found to vary based on conditions such as vanadium ion concentration, acid concentration, electrode material, electrode surface preparation and electrochemical methods used. For the vanadium ions, a decreasing trend of diffusion coefficients with increasing concentration of the vanadium ion and/or acid was found [29,47,48]. The viscosity, however, was found to have an increasing trend [51]. Variation of the kinetic rate constants with concentration, electrode material and electrode surface preparation methods was also seen, but no clear trend could be deduced [49,50].

Sum et al. [44] performed cyclic voltammetry measurements for the VO^{2+}/VO_2^+ couple at low concentrations of vanadium (0.055 M VO_2^+ in 1.8 M H_2SO_4). Wen et al. [47] reported diffusion coefficients for 2 M VO^{2+} in 4 M H_2SO_4. Direct measurements of the VO_2^+ diffusion coefficients were not found for the conditions in the current work. The same are estimated indirectly using the corresponding Stokes radius [48]. The relationship between Stokes radius, viscosity and diffusion coefficient can be expressed as [29]:

$$D_j = \frac{k_b T}{6\pi\mu R_j} \tag{45}$$

where k_b is the Boltzmann constant and R_j is the Stokes radius of species j. For the V^{2+}/V^{3+} couple, Sum et al. [45] and Yamamura et al. [49] report diffusion coefficient measurements at varied solution conditions and electrode materials. However, there is lack of consistent data at the current work's concentration range. Therefore, the diffusion coefficients of V^{2+} and V^{3+} are calculated using their Stokes radii. The viscosity of the acidic vanadium solutions is assumed as 0.008 Pa s for the entire fluid domain as a representative viscosity for all four vanadium species. The charge transfer coefficients (α) for the Butler–Volmer equations are assumed to be 0.5 for both half-cells. A summary of the parameters used for modeling is provided in Tables 1–4.

Table 1
Operating conditions.

Quantity	Symbol	Value	Unit	Source
Operating temperature	T	25	°C	–
Volumetric flow rate	V_{in}^0	1–300	$\mu L\,min^{-1}$	Measured [7]
		1.667×10^{-11} to 5×10^{-9}	$m^3\,s^{-1}$	
Length	L	12×10^{-3}	m	Measured
Width	W	9×10^{-3}	m	Measured
Center channel width	w_c	1×10^{-3}	m	Measured
Inlet reservoir width	w_r	3×10^{-3}	m	Measured
Inlet channel area	a_{in}	6×10^{-7}	m^2	Measured

Table 2
Electrolyte properties.

Quantity	Symbol	Value	Unit	Source
Density	ρ	1200	$kg\,m^{-3}$	[29,51]
Viscosity	μ	0.008	Pa s	[29,47,48]
VO_2^+ diffusion coefficient	D_V	0.364×10^{-10}	$m^2\,s^{-1}$	[29,47,48]
VO^{2+} diffusion coefficient	D_{IV}	0.364×10^{-10}	$m^2\,s^{-1}$	[29,47,48]
V^{3+} diffusion coefficient	D_{III}	0.240×10^{-10}	$m^2\,s^{-1}$	Estimated
V^{2+} diffusion coefficient	D_{II}	0.240×10^{-10}	$m^2\,s^{-1}$	Estimated

Table 3
Electrode properties.

Quantity	Symbol	Value	Unit	Source
Active length	L	12×10^{-3}	m	Measured
Width	w_e	1×10^{-3}	m	Measured
Thickness	h	300×10^{-6}	m	[54]
Porosity	ε	0.78	–	[54]
Fibre diameter	d	7×10^{-6}	m	[22]
Pore diameter	d_p	28×10^{-6}	m	Estimated [23]
Permeability	K	2.375×10^{-11}	m^2	[22]
Electrode platform area	A	1.2×10^{-5}	m^2	Measured
Specific surface area	a	8.333×10^4	m^{-1}	Estimated
Electrical conductivity (in-plane)	σ_s^{eff}	1.15×10^4	$S\,m^{-1}$	[22]

2.5. Solution procedure

The modeling framework described in the previous sections is solved based on conservation of mass, momentum, species and charge. Eqs. (1)–(4) are first solved for the velocity and pressure distributions in the microchannels and porous media. Eq. (5) is then solved for the concentration of each of the four vanadium species together with the charge conservation equation (Eq. (6)) to find the electrode and electrolyte potentials and current densities at a given applied cell potential. The source terms for species and charge conservation are coupled through Eqs. (26) and (27). This coupling also defines the relationship between surface and bulk concentrations (Eqs. (28)–(31)). The numerical simulations are performed using the COMSOL multiphysics code which utilizes a Finite Element Method (FEM) formulation. A quadratic discretization scheme is used for all the mass transport and electrochemical variables. The coupling of the source terms between the mass transport and electrochemistry sub-models introduces non-linearity and makes the solution procedure highly sensitive to the initial values provided. Therefore, in order to achieve stable and fast convergence, the COMSOL segregated solver is employed. The MUMPS direct linear solver is used for all three sub-models. A structured mesh with boundary layers is used for both the 3D and 2D models, and mesh independence and convergence are ensured. The total current density is obtained by numerical integration of the normal electrode current density over the current collector boundary:

$$i_{cell} = \frac{h}{A}\int_{x_1}^{x_2} (\vec{\imath}_s.\hat{n})\,dx \tag{46}$$

where h and A are the electrode thickness and platform area, respectively [7]. A similar numerical integration of concentration at the outlet boundary is performed to calculate the single pass fuel utilization:

$$\varepsilon_{fuel} = \frac{1}{x_3 - x_2}\int_{x_2}^{x_3}\left(\frac{c_{III}}{c_{II}^0}\right)dx \tag{47}$$

The solution procedure is repeated over a selected range of applied cell or electrode potentials to obtain complete performance curves. Typical solution times for the 3D and 2D models are around 15 and 2 h, respectively, on a standard PC.

3. Results and discussion

3.1. Model validation

The present computational model is developed based on the design of the microfluidic fuel cell with flow-through porous electrodes previously reported by our group [7]. To characterize the fundamental physicochemical phenomena and performance of both individual half-cells (anode and cathode) as well as the combined cell, simulations are performed for the entire range of flow rates considered in the experiments, i.e. 1–300 $\mu L\,min^{-1}$. The first step in the model validation process is to validate the 2D simplification introduced in Section 2.1 to reduce the computational time and resources required for the simulations. To achieve this, the modeling of mass transport and electrochemical reactions for a 2D slice are compared to a full 3D model of the cell. Using 3D modeling results as the basis, the relative deviation between the 2D and 3D models, averaged over the modeling domain, is found to be less than 2% when compared using *XY* distributions of electrode

Table 4
Electrochemical parameters.

Quantity	Symbol	Value	Unit	Source
Standard equilibrium potential (vs. SCE)	U_1^0	0.75	V	[30]
Standard equilibrium potential (vs. SCE)	U_2^0	−0.496	V	[30]
Standard rate constant	k_1	6.8×10^{-7}	$m\,s^{-1}$	[49]
Standard rate constant	k_2	1.7×10^{-7}	$m\,s^{-1}$	[45]
Charge transfer coefficient (VO^{2+}/VO_2^+-cathodic reaction)	$\alpha_{1,c}$	0.5	–	Assumed
Charge transfer coefficient (VO^{2+}/VO_2^+-anodic reaction)	$\alpha_{1,a}$	0.5	–	Assumed
Charge transfer coefficient (V^{2+}/V^{3+}-cathodic reaction)	$\alpha_{2,c}$	0.5	–	Assumed
Charge transfer coefficient (V^{2+}/V^{3+}-anodic reaction)	$\alpha_{2,a}$	0.5	–	Assumed

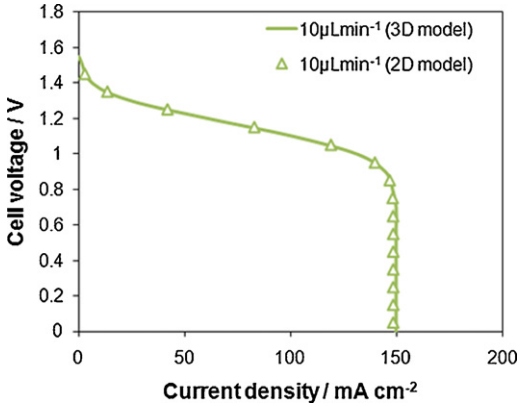

Fig. 2. Comparison of simulated polarization curves from 2D and 3D modeling methodology at a moderate flow rate.

current density. The deviation is found mainly near the channel walls, where the boundary layer predictions of the 3D model lead to lower current densities as compared to the 2D model. The two modeling approaches are also compared using concentration and overpotential distributions which show the same relative deviation as mentioned above. Polarization curves resulting from the two approaches are presented in Fig. 2, again indicating a very close agreement. Other flow rate cases were also simulated to confirm these trends, thus fully justifying the 2D simplification of the proposed model. In subsequent sections, results based on mass transport and electrochemistry are discussed using a 2D slice (Fig. 1(b)) of the electrodes and center channel at the symmetry z-plane, whereas the entire 3D geometry is used to discuss fluid flow.

Next, we seek to validate the numerical model with experimental data from our previous study [7]. For a relevant comparison of simulated and measured data, the external ohmic resistance of the particular fuel cell used for the measurements must first be assessed and added to the modeling parameters, provided it is not captured within the modeling domain described in Fig. 1. In the measurements reported previously [7], the electrical contact between the carbon electrodes and external wires was made using conductive silver epoxy, which is expected to result in a sizeable contact resistance owing to the highly porous nature of the electrode surface. A simple procedure is used to estimate the external resistance from the total ohmic cell resistance measured by Electrochemical Impedance Spectroscopy (EIS) [7]. The internal ohmic resistance is first calculated based on electrode and electrolyte conductivities (Table 3 and Eqs. (33) and (34)) and the average current path inside the cell. This results in an estimated internal ohmic resistance (electrode and electrolyte) of 5.9 Ω. The total ohmic resistance of the cell, including external contacts and wires, was measured to be 31 Ω using EIS [7]. Using this value with the internal resistance estimated above, the external resistance is calculated to be 25.1 Ω. Thus, a value of 25.1 Ω is added externally to the model in order to compare with the specific experimental setup in [7]. A similar procedure can be adopted to estimate the external resistance for a different setup.

After adding the external resistance, the simulated results can be effectively compared to the measured data. It is important to note that these comparisons are based on zero dimensional data such as polarization curves, power density and fuel utilization since measured 2D distributions of concentration, overpotential and current density are not presently available. In Fig. 3(a) and (b), the results of half-cell simulations for the 10 and 60 μL min^{-1} flow rates are compared to the corresponding measured polarization data. Complete cell simulations compared to measurements for both low (1 and

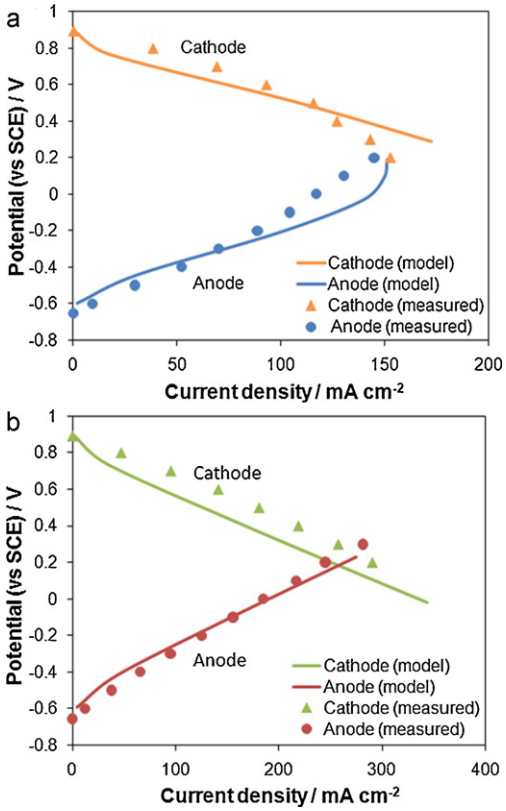

Fig. 3. Comparison of half-cell polarization curves predicted by the model with measurements in [7]: (a) 10 μL min^{-1} flow rate case; and (b) 60 μL min^{-1} flow rate case.

10 μL min^{-1}) and high (60 and 300 μL min^{-1}) flow rates are shown in Fig. 4. It can be seen that good agreement is achieved for both half-cell and fuel cell polarization curves across the whole range of flow rates considered. The agreement is seen to be closer at higher flow rates as the sensitivity of the model to mass transport parameters is lower in this region. The average relative deviation between model and measurements across all flow rates considered is about 10%. The maximum deviation is found to be 19% in the 10 μL min^{-1} case. Figs. 5 and 6 show comparisons for power density and fuel utilization with measurements. Good agreement is observed, with the same relative deviation as mentioned above. The model gives a good estimate of the peak power density point as well as maximum fuel utilization.

Initial measurements based on new cells built in our recently established lab at Simon Fraser University are also included in this study for comparison. These cells are comparable in design to the cell built at the University of Victoria [7], however, the channel and electrode thicknesses are now reduced to 180 μm as compared to 300 μm in the previous work. As shown in Fig. 7, good agreement is again observed for both moderate and high flow rates. The model is seen to follow the measured trends even more closely for this set of data. The relative deviation is found to be less than 10% for the flow rates considered.

It is important to gain an understanding of the general trends and deviations that exist between model and measurements. Some of the prominent features and possible reasons for the deviations are:

1. Uncertainty in kinetic and mass transport parameters obtained from measured values reported in literature. No tuning parameters are used in the present model to ensure general applicability with respect to cell chemistry and design.

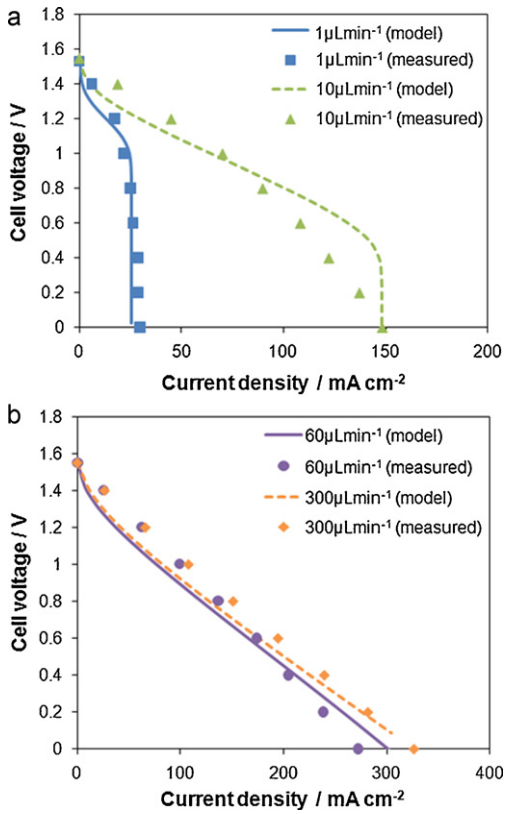

Fig. 4. Comparison of fuel cell polarization curves predicted by the model with measurements in [7] at four different flow rates: (a) 1, 10 (μL min^{-1}); and (b) 60, 300 (μL min^{-1}).

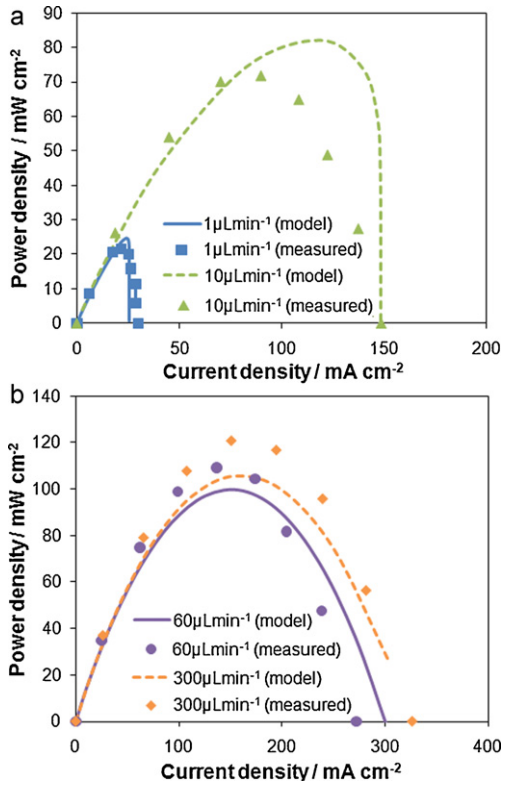

Fig. 5. Predicted power density curves compared to measurements in [7]: (a) 1, 10 (μL min^{-1}) flow rates; and (b) 60, 300 (μL min^{-1}) flow rates.

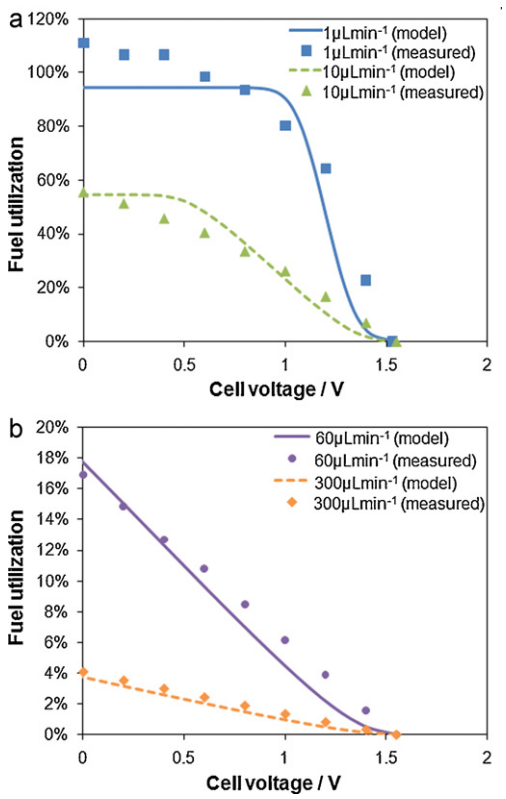

Fig. 6. Predicted fuel utilization as a function of cell voltage, compared to measurements in [7]: (a) 1, 10 (μL min^{-1}) flow rates; and (b) 60, 300 (μL min^{-1}) flow rates.

2. Uncertainty in the convective mass transfer correlation (Eq. (21)) of the order of 30% [38].
3. The model assumes a uniform pore size distribution in the electrodes, whereas in reality the carbon paper material employed is known to exhibit a high degree of anisotropy and a wide range of characteristic pore sizes evident from microscope images and porosimetry measurements [39,52]. This may cause channelling of the flow through predominantly large pores and reduced performance in the mass transport limited regime.
4. The small deviation at low current densities may be due to the assumption of single electron transfer kinetics for the vanadium reactions [26].

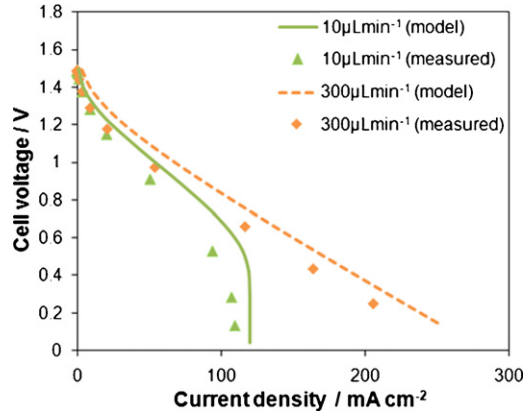

Fig. 7. Comparison of fuel cell polarization curves predicted by the model to new measurements.

In sum, although some minor deviations are found between simulated and measured data, the model is shown to predict the trends observed in measurements within a reasonable tolerance limit and provides useful estimates of half-cell and cell polarization, power density and fuel utilization over the entire range of current densities and flow rates considered.

While the fuel cells in [7] displayed large external resistances, efforts currently underway at our lab indicate that the external resistance can be brought down to a value close to 10 Ω. In subsequent sections, the results are discussed based on the computational model with this external resistance added. This is to ensure that the modeling results take into account the issue of large contact resistances which are present in these cells and at the same time maintain generality in the discussions and conclusions. In adapting these general results to a specific case, it is advisable to measure external resistances for the specific experimental setup and adjust predicted voltages accordingly. The results are discussed for two main operating conditions: (1) maximum efficiency point; and (2) limiting current density point (mass transport limit).

3.2. Effect of flow distribution

The 3D flow distribution in the electrodes and inlet/outlet channels is analyzed for uniformity. Larger cross-flow velocity magnitudes (in the x direction) are seen in the portions of the electrodes near the outlet. These magnitudes are found to be up to 2.5 times higher than those near the current collectors. This non-uniformity is mainly attributed to the center channel which is narrower in width as compared to the inlet channels (Fig. 1(a)) thereby contributing a larger pressure drop. This is expected to impact the concentration and potential distributions in the cell due to differences in rate of mass transfer. Flow within the porous electrodes is effectively uniform in the z-direction due to the plug flow conditions occurring when the pore size is significantly smaller than the channel height. For the same reason, boundary layers within the electrode are found to be small compared to those in the free channel.

The parasitic pumping power required to drive the electrolyte flow can be analyzed based on the simulated pressure drops in the microfluidic channels and porous electrodes of the cell and subtracted from the total power produced. The total pumping power is determined by the product of the pressure drop (from inlet to outlet) and the volumetric flow rate for the two streams:

$$P_{pump} = 2\Delta p V_{in}^{0} \tag{48}$$

For the 10 μL min^{-1} case, the pumping power is found to be 6.46×10^{-6} mW and for the 300 μL min^{-1} case it is 5.82×10^{-3} mW. The fraction of total pumping power to corresponding power output of the cell is thus less than 0.1% in all cases considered, and can therefore be neglected.

3.3. Cell performance and optimum operating point

Fig. 8 presents the half-cell and complete cell polarization curves obtained by the model, representing the theoretical performance of the fuel cell for the case of 10 Ω external contact or wire resistances. It can be seen from Fig. 8(a) that the anode is the limiting electrode in the present case. The reason for this lies in the lower diffusion coefficient values of the anode side vanadium species as compared to the cathode which means that transport to and from the electrode is slower on the anode side, leading to a lower limiting current density compared to the cathode. As seen in Fig. 8(b), the polarization curves for all flow rates considered display three distinct regions: an activation loss region at low current densities; a constant ohmic slope at mid-range current densities; and a limiting

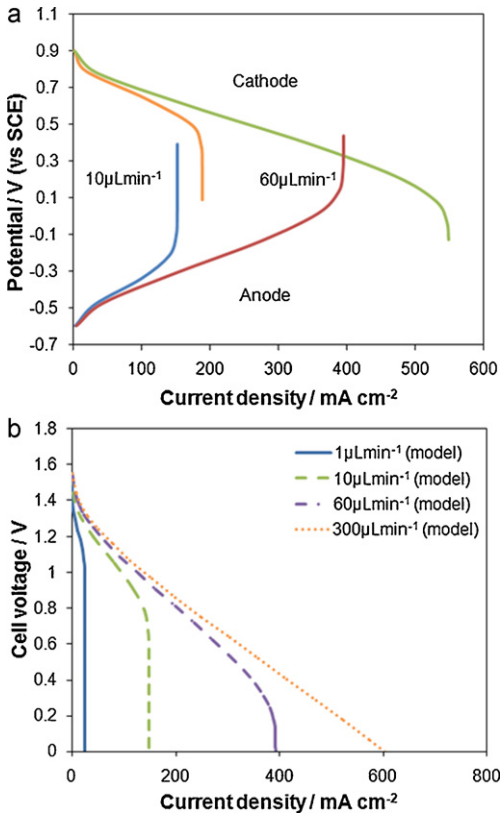

Fig. 8. Predicted theoretical polarization curves with external resistance of 10 Ω: (a) half-cell polarization curves for 10 and 60 (μL min^{-1}); and (b) fuel cell polarization curves for 1, 10, 60 and 300 (μL min^{-1}) flow rates.

current drop at high current densities. The limiting current region is generally present except at the highest flow rate (Fig. 8(b)) considered here where the large ohmic polarization causes the voltage to drop to zero before the limiting current density is attained. The limiting current value follows a general trend with flow rate consistent with a Levich type relation. Due to the high in-plane conductivity of the carbon paper electrodes combined with a high concentration of supporting electrolyte, the cell is expected to have a low internal resistance as reflected in the gentle slopes in the ohmic region of the curves. These findings indicate that even with flow-through porous electrodes the mass transport to the active sites is still the main constraint to cell performance (under the assumption that the external contact resistances can be reduced to a moderate value (<10 Ω)).

Power density and single pass fuel cell efficiency are two of the most relevant performance metrics for microfluidic fuel cells with flow-through porous electrodes, and for most applications it is desirable to achieve concurrently high levels of these two characteristics. In the present flow-through case, the power density is determined by the product of current density and cell voltage, while the single pass fuel cell efficiency is determined by the product of current and voltage efficiencies. Provided that only the main vanadium redox reactions (Eqs. (7) and (8)) are considered in the model, the current efficiency is equal to the fuel utilization, as given by:

$$\varepsilon_i = \varepsilon_{fuel} = \frac{i_{cell} A}{V_{in}^{0} F c_{II}^{0}} \tag{49}$$

The voltage efficiency based on the standard cell voltage of $U_{cell}^{0} = 1.246$ V is given by:

$$\varepsilon_V = \left(\frac{V_{cell}}{U_{cell}^{0}} \right) \tag{50}$$

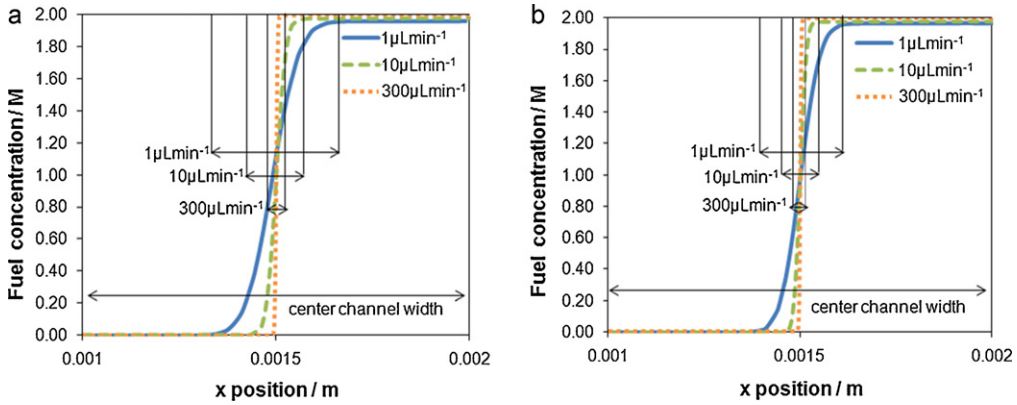

Fig. 9. Concentration distribution of V^{2+} (fuel) across the center channel at (a) an upstream location ($y = L$) and (b) a downstream location ($y = 0$), for 1, 10 and 300 ($\mu L\,min^{-1}$) flow rates at OCV conditions.

The single pass fuel cell efficiency then becomes:

$$\varepsilon_{cell} = \varepsilon_i \times \varepsilon_V = \frac{V_{cell} i_{cell} A}{U^0_{cell} V^{in}_0 Fc^0_{II}} \tag{51}$$

In coherence with the power density, the single pass efficiency is thus proportional to the product of current density and cell voltage. Consequently, the theoretical maximum power density and single pass efficiency of the microfluidic fuel cell always occur at the same operational point on the polarization curve. This favourable performance characteristic greatly simplifies cell design and operation as the optimum point for power and efficiency is shared. In the present modeling study, the maximum cell efficiency is found to be 77% for 1 $\mu L\,min^{-1}$ at a cell voltage of 1.1 V. The efficiency is found to peak at high cell voltages for low flow rates and at moderate voltages for high flow rates, attributed to the high current densities and subsequently high ohmic losses at high flow rates. At the maximum efficiency point, the theoretical power densities increase with flow rate from 26 $mW\,cm^{-2}$ for 1 $\mu L\,min^{-1}$ to 193 $mW\,cm^{-2}$ for 300 $\mu L\,min^{-1}$. The high power densities may in some cases justify operation of the cell at high flow rates despite the low efficiencies (<10%), e.g., for applications having high power requirements for short durations, while a notable power density trade-off is evident for operation in the highly efficient low flow rate regime. In sum, the high theoretical levels of cell efficiency and power density predicted by the model, and the fact that these two characteristics share the same optimum operating point at a given flow rate, is encouraging towards further development of this technology.

3.4. Secondary reactions

At low flow rates close to 1 $\mu L\,min^{-1}$, the model predicts a lower limiting current density than the experimental measurements (Fig. 4(a)) which tend to deviate slightly from the vertically drooping polarization curve characteristic of the mass transfer limit. In addition, the measurements at 1 $\mu L\,min^{-1}$ show fuel utilization greater than 100% (Fig. 6(a)) [7]. This is likely attributed to the secondary V^{3+}/VO^{2+} redox reactions observed in measurements at cell voltages below 0.4 V [7]. The modeling results are used to analyze the extent and effects of this reaction. Local overpotentials at the cathode and anode are calculated for the V^{3+}/VO^{2+} couple (Eq. (9)) as: $\eta = \phi_s - \phi_l - U$, where $U = 0.07$ V vs. SCE [30]. At low flow rates and high current densities (low cell voltages), increased fuel utilization results in relatively high concentrations of product VO^{2+} and V^{3+} at the cathodic and anodic side, respectively. Owing to the relatively large electrochemical potential gap between the secondary reaction and the two primary reactions (0.57 and 0.68 V for anode and cathode, respectively), sufficiently high overpotentials required for the secondary reaction to occur are only found for cell voltages below ~0.6 V. At this cell voltage, the concentration of product VO^{2+} and V^{3+} averaged over the respective electrode area is found to be 1.4 M, which is high enough to drive the reaction forward kinetically. Thus, both thermodynamic and kinetic conditions for the secondary reaction are satisfied when the cell is operated at concurrently low levels of flow rate and cell voltage. It is noteworthy, however, that the secondary reaction is negligible over the majority of the operational range of the cell, including its optimum performance point at peak power and maximum efficiency.

3.5. Concentration distribution and crossover

The inter-diffusive mixing between the two stratified streams in the center channel is analyzed under simulated open circuit voltage (OCV) conditions at the lowest flow rate, where the fuel and oxidant concentrations are the highest and diffusive mixing is most severe. The concentration variation of V^{2+} (fuel) across the width of the center channel at an upstream ($y = L$) and downstream ($y = 0$) location is plotted in Fig. 9(a) and (b), respectively. It is evident that even for the extreme case of 1 $\mu L\,min^{-1}$ flow rate at OCV conditions the mixing width is small compared to the width of the center channel. Further, the mixing width decreases along the length of the center channel (Fig. 9(a) and (b)). This seemingly counter-intuitive but favourable result is however a unique feature of this flow-through electrode architecture. In contrast to the planar or Y-channel fuel cell designs [20,53], the fluid velocity increases with downstream position along the center channel, i.e., towards the outlet, due to the relatively uniform cross-flow through the electrodes. As shown in Fig. 9, the mixing width is even smaller for the higher flow rates considered.

On computing the crossover flux from one electrode to the other, a second favourable feature of the unique flow-through architecture is discovered. In the present case, the flow taking place at the porous electrode/center channel interface is orthogonal to the principal axis of the center channel, in contrast to earlier cell architectures [9–12,14] where the flow is predominantly parallel to the principal axis in flow-by (or flow-over) mode. Due to the flow-through configuration, any crossover flux from one electrode towards the other thus needs to diffuse upstream into the opposite electrolyte flow in order to reach the opposite electrode and contribute towards secondary reactions. A net upstream diffusive flux can only occur when the convective flux in the flow direction is lower than the upstream rate of diffusion. The resulting Peclet number for crossover flux is defined based on channel height:

$$Pe_{co} = \frac{(\vec{v}.\hat{n})h}{D_j} \tag{52}$$

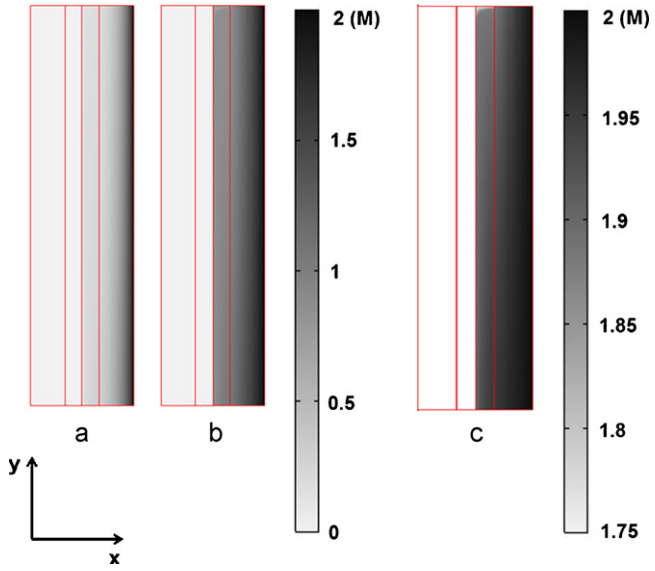

Fig. 10. Concentration profiles of V^{2+} (fuel) in the symmetry z-plane at selected operating conditions corresponding to the maximum efficiency point at three different flow rates: (a) 1 μL min^{-1}; (b) 10 μL min^{-1}; and (c) 300 μL min^{-1}.

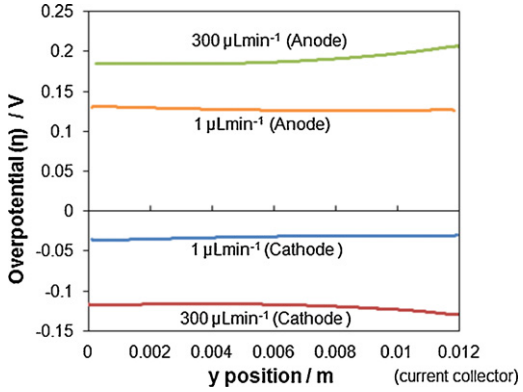

Fig. 11. Overpotential (η) distributions along the electrode length for cell operation at the maximum efficiency point (obtained at the midpoint of the electrode width).

where $\vec{v} \cdot \hat{n}$ denotes the flow velocity normal to the electrode boundary ($x = x_3$, Fig. 1(a)) and D_j is the diffusion coefficient of a given vanadium species. Upstream diffusion is expected to occur when the Peclet number defined above is less than unity. Simulations of the fuel cell carried out at very low flow rates (<1 μL min^{-1}) confirm this presumption. The diffusion dominated regime is found to set in at flow rates below 0.02 μL min^{-1}, corresponding to a Peclet number of 0.1. At flow rates above this value the net flux into the electrodes drops sharply with increasing flow rate due to the convection dominated mass transport. For the case of 1 μL min^{-1} flow rate at OCV conditions, the net flux of primary reactant into the electrode is computed to be three orders of magnitude greater than the crossover flux. Consequently, crossover flux and associated parasitic secondary current can be safely neglected for the cell geometry and flow rates considered in this study.

The concentration plot for 1 μL min^{-1} flow rate obtained at the maximum efficiency point (Fig. 10(a)) shows that most of the fuel is consumed before the cross-flow exits the electrode into the center channel. Furthermore, a major contribution for the reaction appears to occur in the entrance portion of the electrode where the reactant concentration is high. The concentration profile for this case also reveals that the electrode is underutilized for this flow rate since half of the electrode width contributes to 90% of the conversion. In Fig. 10(b), decreased fuel conversion at increased flow rates is observed for the 10 μL min^{-1} case. As flow rates increase, the higher current densities are expected to make ohmic polarization a more dominant factor. In Fig. 10(c) for the 300 μL min^{-1} flow rate, the fuel conversion is greater near the current collector as compared to the portion of the electrode near the outlet, owing to the ohmic potential drop along the electrode length. In addition, the overall consumption of fuel is notably smaller at this flow rate.

3.6. Electrode performance at maximum efficiency

The simulated electrode performance characteristics are analyzed in more detail for operation at the maximum efficiency point. The local overpotential is plotted along the electrode length for a low (1 μL min^{-1}) and high (300 μL min^{-1}) flow rate in Fig. 11. Increase in ohmic polarization effects with increased flow rate is evident due to larger current densities generated at higher flow rates. At low and moderate flow rates the distributions have a negligible gradient along the electrode length, whereas they show clear variation along the length for high flow rates (Fig. 11). For the 300 μL min^{-1} case, the difference in overpotential between the current collector and the opposite end of the electrode is on the order of 10–100 mV, which causes the trend in fuel conversion explained above (Section 3.5). The local overpotential in the electrode is one of

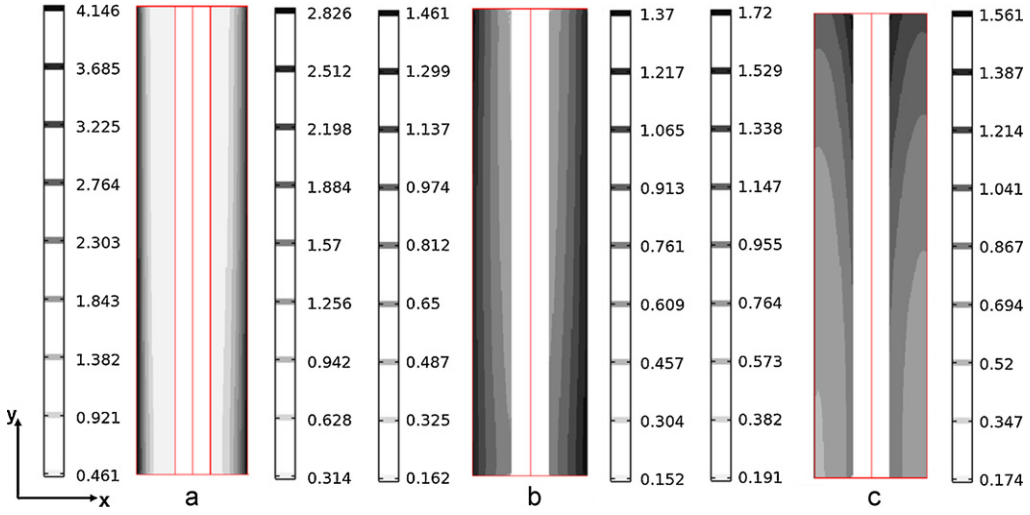

Fig. 12. Normalized current density distributions in the symmetry z-plane at the maximum efficiency point: (a) 1 μL min^{-1}; (b) 10 μL min^{-1}; and (c) 300 μL min^{-1}.

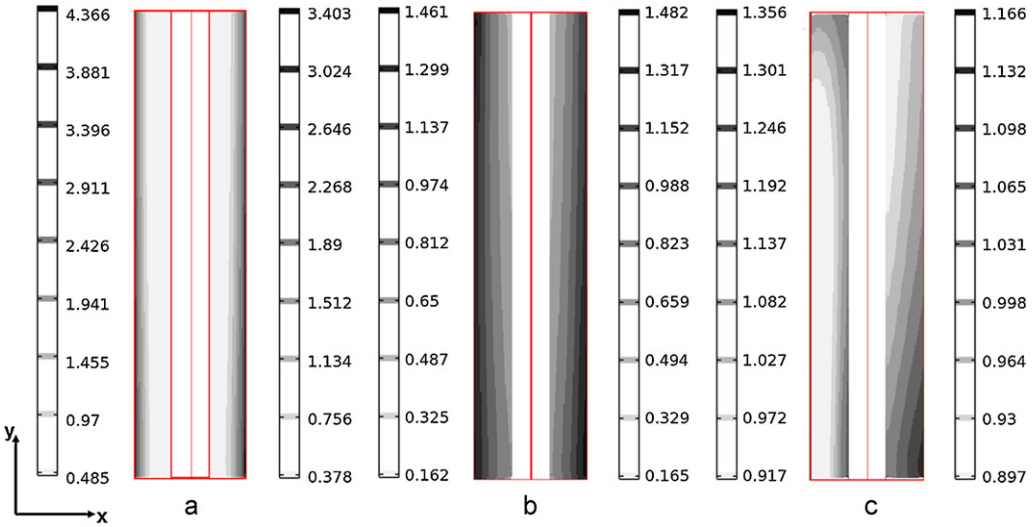

Fig. 13. Normalized current density distributions in the symmetry z-plane at the limiting current density: (a) 1 μL min^{-1}; (b) 10 μL min^{-1}; and (c) 300 μL min^{-1}.

the parameters governing the reaction rate or local current density at that point, which is an indicator of electrode performance. Other factors are the local velocity magnitude, concentration difference between and bulk and surface, as well as the reaction rate constants. To understand the combined effect of these, the normalized current density, or source term (S_1 and S_2), is plotted for the three different flow rates in Fig. 12. This current density is normalized by dividing by its average value over the entire electrode platform area. For the cathode and anode side it is given as:

$$J_1^n = \frac{|ai_1|}{\int\int(|ai_1|/Lw_e)\cdot dA} \tag{53}$$

$$J_2^n = \frac{|ai_2|}{\int\int(|ai_2|/Lw_e)\cdot dA} \tag{54}$$

As per the normalization method, local values greater than the average translate to normalized values greater than unity and vice versa. For ideal, uniform electrode performance, the normalized values should be close to unity everywhere in the electrode. In Fig. 12(a) and (b), representing low and moderate flow rates, a visible band of high local current density values is observed at the entrance of the electrode. The contours at low flow rates (hence low current densities) also indicate that the concentration difference between bulk and surface is the main factor that influences the variations in local current density along the electrode. At high flow rates, however, the overpotential is found to play a more important role, with the reaction current density having a larger value near the current collectors (Fig. 12(c)).

3.7. Electrode performance at limiting current

It is interesting to see if the trends discussed above at maximum efficiency also hold when one or both of the electrodes is producing the maximum or limiting current density for a given flow rate. Once again the normalized current density is utilized as a cumulative indicator of the various factors mentioned above. The results in Fig. 13(a) and (b) are similar to the maximum efficiency plots at low and moderate flow rates, however, a reversal in trends is found at high flow rates. At low and moderate flow rates, the performance is predominantly mass transport controlled at both maximum efficiency and limiting current density points, and exhibits a slightly greater current contribution from the region of the electrodes with greater local velocities. At high flow rates, it was discussed above that the overpotential effects dominate hence leading to greater contribution from the regions near the current collector. The opposite effect is found at the limiting current density point, where the regions experiencing greater flow velocities (Section 3.2) display larger reaction source terms despite the relatively low overpotential magnitudes. This reversed trend is only observed in the anode, which is presently the limiting electrode of the cell. It is deduced from this observation that local velocities play a significant role in determining the electrode performance at the limiting current density point.

4. Conclusions

A detailed computational model of a microfluidic fuel cell with flow-through porous electrodes is developed and validated. The present model is the first comprehensive, cell-level model of this fuel cell architecture. The three major coupled phenomena occurring in the cell, namely the fluid flow, mass transfer and electrochemical kinetics, are solved in 3D using a computational multiphysics solver. Performance measurements carried out on these cells are used to validate the resulting model. The modeling results are found to be in good agreement with experimental data over three orders of magnitude of flow rates and current densities spanning the complete operational range of these devices. The results are employed to verify and quantify the relatively high external contact resistance of the present prototype cells. With a representative external resistance of 10 Ω, the model predicts that theoretical efficiencies up to 77% and power densities up to 193 mW cm^{-2} are feasible at low and high flow rates, respectively. Interestingly, the maximum efficiency and peak power of this technology are found to share the same optimum operational point on the polarization curve at a given flow rate. Furthermore, the modeling results indicate that secondary reactions and reactant crossover can be neglected for the cell architecture and operating conditions considered in this study.

An initial investigation is carried out using the validated model to identify variations in performance within the porous electrodes. The analysis based on simulated spatial distributions of concentration, overpotential and current density reveals some interesting and useful trends. Local concentration variations determine electrode performance for low and moderate flow rates, indicating mass transfer controlled operation. At high flow rates, both mass transfer and ohmic effects are significant, and highly coupled trends

are observed. Cell design attributes such as optimal width or active area of the electrode to achieve high fuel utilization (>90%) are thus highly dependent on flow rate even for porous flow-through architectures.

Based on our preliminary investigation, we can conclude that performance increases are possible by using modeling results to drive the fuel cell design cycle. Some possible areas of improvement include modifying the electrode and channel geometries to reduce ohmic polarization effects and optimizing the electrolyte flow path based on flow rate and required power density. These increases are over and above those achieved by solving the contact resistance problem which is presently the main bottleneck for performance improvement. The model is thus useful for both performance predictions and scientific studies to gain a clear understanding between the interplay of various physicochemical mechanisms and their effect on cell performance. The model is also anticipated to become a useful tool for design and analysis of other fuel cells and electrochemical sensors which incorporate microfluidic flow-through porous electrodes. A detailed parametric analysis of the flow-through microfluidic fuel cell based on the model developed here will be presented in a forthcoming work.

Acknowledgments

Funding for this research provided by the Natural Sciences and Engineering Research Council of Canada, MITACS, Western Economic Diversification Canada, Canada Foundation for Innovation, British Columbia Knowledge Development Fund, and Simon Fraser University is highly appreciated. We are indebted to Dr. Clive Brereton at NORAM Engineering and Constructors Ltd., and Mr. Peter Hsiao and Mr. Larry Hoang at SFU for assistance in experimentation and measurements.

References

[1] S. Pennathur, J.C.T. Eijkel, A. van den Berg, Lab on a Chip 7 (2007) 1234–1237.
[2] G.J. La O, H.J. In, E. Crumlin, G. Barbastathis, Y. Shao-Horn, International Journal of Energy Research 31 (2007) 548–575.
[3] V. Grinberg, A. Skundin, Russian Journal of Electrochemistry 46 (2010) 963–978.
[4] E. Kjeang, N. Djilali, D. Sinton, Journal of Power Sources 186 (2009) 353–369.
[5] S.A. Mousavi Shaegh, N.-T. Nguyen, S.H. Chan, International Journal of Hydrogen Energy 36 (2011) 5675–5694.
[6] J.C. McDonald, D.C. Duffy, J.R. Anderson, D.T. Chiu, H.K. Wu, O.J.A. Schueller, G.M. Whitesides, Electrophoresis 21 (2000) 27–40.
[7] E. Kjeang, R. Michel, D.A. Harrington, N. Djilali, D. Sinton, Journal of the American Chemical Society 130 (2008) 4000–4006.
[8] M. Skyllas-Kazacos, F. Grossmith, Journal of the Electrochemical Society 134 (1987) 2950–2953.
[9] R. Ferrigno, A.D. Stroock, T.D. Clark, M. Mayer, G.M. Whitesides, Journal of the American Chemical Society 124 (2002) 12930–12931.
[10] E.R. Choban, L.J. Markoski, A. Wieckowski, P.J.A. Kenis, Journal of Power Sources 128 (2004) 54–60.
[11] J.L. Cohen, D.A. Westly, A. Pechenik, H.D. Abruna, Journal of Power Sources 139 (2005) 96–105.
[12] R.S. Jayashree, L. Gancs, E.R. Choban, A. Primak, D. Natarajan, L.J. Markoski, P.J.A. Kenis, Journal of the American Chemical Society 127 (2005) 16758–16759.
[13] E. Kjeang, J. McKechnie, D. Sinton, N. Djilali, Journal of Power Sources 168 (2007) 379–390.
[14] E. Kjeang, B.T. Proctor, A.G. Brolo, D.A. Harrington, N. Djilali, D. Sinton, Electrochimica Acta 52 (2007) 4942–4946.
[15] K.S. Salloum, J.R. Hayes, C.A. Friesen, J.D. Posner, Journal of Power Sources 180 (2008) 243–252.
[16] K.S. Salloum, J.D. Posner, Journal of Power Sources 195 (2010) 6941–6944.
[17] K.S. Salloum, J.D. Posner, Journal of Power Sources 196 (2011) 1229–1234.
[18] A. Bazylak, D. Sinton, N. Djilali, Journal of Power Sources 143 (2005) 57–66.
[19] M.-H. Chang, F. Chen, N.-S. Fang, Journal of Power Sources 159 (2006) 810–816.
[20] F.L. Chen, M.H. Chang, M.K. Lin, Electrochimica Acta 52 (2007) 2506–2514.
[21] B. Bird, W. Stewart, E. Lightfoot, Transport Phenomena, Wiley, 2006.
[22] J. Becker, R. Fluckiger, M. Reum, F.N. Buchi, F. Marone, M. Stampanoni, Journal of the Electrochemical Society 156 (2009) B1175–B1181.
[23] M.M. Tomadakis, T.J. Robertson, Journal of Composite Materials 39 (2005) 163–188.
[24] D. You, H. Zhang, J. Chen, Electrochimica Acta 54 (2009) 6827–6836.
[25] A.A. Shah, M.J. Watt-Smith, F.C. Walsh, Electrochimica Acta 53 (2008) 8087–8100.
[26] C. Fabjan, J. Garche, B. Harrer, L. Jörissen, C. Kolbeck, F. Philippi, G. Tomazic, F. Wagner, Electrochimica Acta 47 (2001) 825–831.
[27] M. Gattrell, J. Park, B. MacDougall, J. Apte, S. McCarthy, C.W. Wu, Journal of the Electrochemical Society 151 (2004) A123–A130.
[28] M. Gattrell, J. Qian, C. Stewart, P. Graham, B. MacDougall, Electrochimica Acta 51 (2005) 395–407.
[29] G. Oriji, Y. Katayama, T. Miura, Electrochimica Acta 49 (2004) 3091–3095.
[30] CRC Handbook of Chemistry and Physics, 83rd ed., CRC Press, Boca Raton, FL, 2002.
[31] A.J. Bard, M. Stratmann, C.J. Pickett (Eds.), Encyclopedia of Electrochemistry, Inorganic Chemistry, Wiley, John & Sons, 2006.
[32] Gao et al. In: 217th ECS Meeting, The Electrochemical Society, 2010.
[33] M. Saleh, Journal of Solid State Electrochemistry 11 (2007) 811–820.
[34] A.A. Shah, H. Al-Fetlawi, F.C. Walsh, Electrochimica Acta 55 (2010) 1125–1139.
[35] J. Larminie, A. Dicks, Fuel Cell Systems Explained, John Wiley & Sons Inc., Hoboken, NJ, 2003.
[36] M.M. Mench, Fuel Cell Engines, Wiley, New York, 2008.
[37] H. Al-Fetlawi, A.A. Shah, F.C. Walsh, Electrochimica Acta 55 (2009) 78–89.
[38] D. Schmal, J. Van Erkel, P.J. Van Duin, Journal of Applied Electrochemistry 16 (1986) 422–430.
[39] N. Zamel, X. Li, J. Shen, Energy & Fuels 23 (2009) 6070–6078.
[40] P.K. Das, X. Li, Z.-S. Liu, Applied Energy 87 (2010) 2785–2796.
[41] R. Flückiger, S.A. Freunberger, D. Kramer, A. Wokaun, G.G. Scherer, F.N. Büchi, Electrochimica Acta 54 (2008) 551–559.
[42] J.G. Pharoah, K. Karan, W. Sun, Journal of Power Sources 161 (2006) 214–224.
[43] D.A.G. Bruggeman, Annalen Der Physik (Leipzig) 24 (1935) 636.
[44] E. Sum, M. Rychcik, M. Skyllas-Kazacos, Journal of Power Sources 16 (1985) 85–95.
[45] E. Sum, M. Skyllas-Kazacos, Journal of Power Sources 15 (1985) 179–190.
[46] S. Zhong, M. Skyllas-Kazacos, Journal of Power Sources 39 (1992) 1–9.
[47] Y.-H. Wen, H.-M. Zhang, P. Qian, H.-P. Ma, B.-L. Yi, Y.-S. Yang, Chinese Journal of Chemistry 25 (2007) 278–283.
[48] G. Oriji, Y. Katayama, T. Miura, Journal of Power Sources 139 (2005) 321–324.
[49] T. Yamamura, N. Watanabe, T. Yano, Y. Shiokawa, Journal of the Electrochemical Society 152 (2005) A830–A836.
[50] H. Kaneko, K. Nozaki, Y. Wada, T. Aoki, A. Negishi, M. Kamimoto, Electrochimica Acta 36 (1991) 1191–1196.
[51] F. Rahman, M. Skyllas-Kazacos, Journal of Power Sources 189 (2009) 1212–1219.
[52] J.T. Gostick, M.W. Fowler, M.D. Pritzker, M.A. Ioannidis, L.M. Behra, Journal of Power Sources 162 (2006) 228–238.
[53] M.H. Chang, F. Chen, N.S. Fang, Journal of Power Sources 159 (2006) 810–816.
[54] TGPH-090, TORAY Industries, www.toray.com.